The DOI for this manuscript is doi: 10.1175/JCLI-D-14-00400.1

The final published version of this manuscript will replace the preliminary version at the above DOI once it is available.

If you would like to cite this EOR in a separate work, please use the following full citation:

Wang, X., C. Wang, L. Zhang, and X. Wang, 2015: Multidecadal Variability of Tropical Cyclone Rapid Intensification in the Western North Pacific. J. Climate. doi:10.1175/JCLI-D-14-00400.1, in press.

Multidecadal Variability of Tropical Cyclone Rapid Intensification in the Western North Pacific

Xidong Wang[*1], Chunzai Wang[2], Liping Zhang[3], Xin Wang[4]

1. Key Laboratory of Marine Environmental Information Technology, SOA, National Marine Data and Information Service, Tianjin 300171, China

2. NOAA/Atlantic Oceanographic and Meteorological Laboratory, Miami, FL, USA

3. Cooperative Institute for Marine and Atmospheric Studies, University of Miami, Miami, FL, USA

4. State Key Laboratory of Tropical Oceanography, South China Sea Institute of Oceanology, Chinese Academy of Sciences, Guangzhou 510301, China

Revision to Journal of Climate

December 2014

*Corresponding author：Xidong Wang
Address: 93 Liuwei Road, Hedong District, Tianjin 300171, China.
E-mail: xidong_wang@yahoo.com
Telephone: 86-22-24010848

Abstract

This study investigates the variation of tropical cyclone (TC) rapid intensification (RI) in the western North Pacific (WNP) and its relationship with large-scale climate variability. RI events have exhibited strikingly multidecadal variability. During the warm (cold) phase of the Pacific decadal oscillation (PDO), the annual RI number is generally lower (higher) and the average location of RI occurrence tends to shift southeastward (northwestward). The multidecadal variations of RI are associated with the variations of large-scale ocean and atmosphere variables such as sea surface temperature (SST), tropical cyclone heat potential (TCHP), relative humidity (RHUM) and vertical wind shear (VWS). It is shown that their variations on multidecadal timescale depend on evolution of the PDO phase. The easterly trade wind is strengthened during the cold PDO phase in the low level, which tends to make equatorial warm water spread northward into the main RI region due to meridional ocean advection associated with Ekman transport. Simultaneously, an anticyclonic wind anomaly is formed in the subtropical gyre of the WNP. This therefore may deepen the depth of 26°C isotherm and directly increase TCHP over the main RI region. These thermodynamic effects associated with the cold PDO phase greatly support RI occurrence. The reverse is true during the warm PDO phase. The results also indicate that the VWS variability in the low wind shear zone along the monsoon trough may not be critical for the multidecadal modulation of RI events.

Keywords: Tropical Cyclone; Rapid Intensification; Multidecadal Variability; Pacific Decadal Oscillation.

1. Introduction

The significant improvements have been made in the forecasting of both tropical cyclone (TC) tracks and intensity over past two decades (DeMaria et al. 2014). However, compared with the forecasting of TC tracks, the forecasting of TC intensity change has been confronted with more enormous challenge, especially the forecasting of TC rapid intensification (RI) (e.g., Elsberry et al. 2007; Rappaport et al. 2009; Chen et al. 2011). The relatively low skill of intensity forecasts is primarily due to the complexity of the TC process, which involves multi-scale interactions between TC and environments in the ocean and atmosphere. TC RI is an essential characteristic of Category 4 and 5 TCs in the Saffir-Simpon scale. Category 4 and 5 TCs are called super typhoons in the western Pacific. 90% of super typhoons in the western North Pacific (WNP; Wang and Zhou 2008) and all Category 4 and 5 hurricanes in the Atlantic basin experience at least one RI process in their lifespan (Kaplan and DeMaria 2003). Better understanding of the RI mechanism will therefore help to reduce the loss caused by TC.

The role of the upper ocean in TC intensification has been identified for several decades (e.g., Leipper 1967). The effect of sea surface temperature (SST) on the TC intensity has better been known. For example, the SST of 26-27°C is found to be the threshold for TC intensification (Chan et al. 2001). SST underlying a TC primarily determines the hurricane maximum potential intensity (Emanuel et al. 2004) which is an important statistical predictor of RI (e.g., Kaplan and DeMaria 2003; Kaplan et al 2010). Recently, tropical cyclone heat potential (TCHP), which represents ocean heat content contained in the water warmer than 26°C, has been shown to reduce the error in intensity forecasts of tropical Atlantic hurricanes when used as a predictor in statistical prediction methods (e.g., Mainelli et al. 2008; Goni et al. 2009). Most of the major Category 4 or 5 TCs in various basins have been found to rapidly intensify over regions of high TCHP associated with warm eddy or the thick and warm mixed layer (e.g., Shay et al. 2000; Lin et al. 2005, 2008, 2009a,b; Ali 2007; Rozoff and Kossin 2011). In regions of high fresh water input where significant salinity stratification sets within a deep isothermal layer, a barrier layer between the base of the isothermal layer and the base of the mixed layer can appears. Several studies have suggested an active role of the barrier layer in TC intensification (e.g., Wang et al. 2011; Balaguru et al. 2012). Generally speaking, the TC-induced SST cooling plays a negative feedback role in TC intensification (e.g., Schade and Emanuel 1999; Cione and Uhlhorn 2003). Therefore, the effects of both the warm eddy and barrier layer on TC intensification may be to limit the reduction of TC-induced SST cooling, which in turn decreases the negative feedback effect from the ocean to atmosphere.

Many studies have emphasized the importance of large-scale atmospheric environmental factors in the RI process. Observational and modeling results indicated that RI is more likely to appear when there is less interaction between a TC and upper-level system (e.g., Emanuel 1999). In the North Atlantic, Kaplan and DeMaria (2003) suggested that RI is located at the regions of low vertical wind shear (VWS), weak upper-level forcing from troughs and high relative humidity of the mid-low troposphere. Ventham and Wang (2007) found that in the WNP, RI is characterized by lower-level monsoon confluence environmental flows which play critical roles in determining RI. Shu et al. (2012) examined the effects of large-scale environmental factors on TC RI in the WNP. It was found that the RI cases have higher low-troposphere relative humidity

(RHUM), lower VWS and more easterly upper-troposphere flow than the non-RI cases.

A great number of investigations have been made to address the influence of climate change on TC activity. It was argued that the recent increase of SST tends to cause the increasing intensity and potential destructiveness of TCs over the past about 30 years (Emanuel 2005). Meanwhile, others have argued that if the time series of TCs is extended to earlier years, the increase in TC intensity is actually part of a multidecadal fluctuation in the frequency of TCs (Landsea 2005; Chan 2006). Some studies have focused on the decadal variations of TC activity in the WNP. Ho et al. (2004) examined the interdecadal variability of the summertime typhoon tracks over the WNP. They divided the 1951-2001 periods into two sub-periods of 1951–79 and 1980–2001, and found that the typhoon passage frequency decreased significantly over the East China Sea and the Philippine Sea, but increased slightly over the South China Sea in the latter period. Examining various thermodynamic and dynamic factors, Chan (2008) found that the frequency and tracks of Categories 4 and 5 TCs in the WNP undergo decadal variations due to variations in global oceanic and atmospheric conditions in association with El Niño-Southern Oscillation (ENSO) and the Pacific Decadal Oscillation (PDO). Yeh et al. (2010) showed a decadal relationship between the TC frequency and tropical Pacific SST, with a positive correlation during the period 1990–2000 but a negative correlation during the period 1979–1989. Liu and Chan (2013) examined changes in TC activity and atmospheric conditions during 1998-2011. TC activity shows a significant decrease, which is partly related to the decadal variation of the TC genesis frequency in the southeastern part of the WNP.

Most of the previous studies mentioned above focused on influence of climate factors on the genesis, tracks, duration and intensity of TCs. Few studies have attempted to examine TC RI variability on multidecadal time scale and associated it with oceanic and atmospheric signals in the WNP. If there are multidecadal fluctuations in TC RI events, it is of key importance to examine the corresponding changes in large-scale environmental factors and to determine whether there is a relationship between them on multidecadal time scale. The present study therefore attempts to examine multidecadal variation of TC RI in the WNP and its possible relationship with climatic signals such as the PDO. This study suggests a new mechanism by which the PDO may modulate large-scale environmental factors to make a contribution to TC RI over the WNP on multidecadal timescale.

The rest of this paper is organized as follows. The data and methodology employed in this paper are shown in section 2. Section 3 presents the climatological distribution of TC RI over the WNP. Section 4 investigates multidecadal variability of RI and the related large-scale environments and their relationship with the PDO. Summary and discussion are given in section 5.

2. Data and methodology

The 6-h best-track data of TCs occurring between 1951 and 2008 over the WNP are obtained from the Joint Typhoon Warning Center, which consist of the 6-h estimates of position, maximum sustained surface wind speed and central pressure. This dataset is used to identify the occurrence of RI. We follow the conventional definition which adopts 95% percentile of over-water intensity changes in 24 hours for all of TCs as a critical value of RI (Kaplan and DeMaria 2003; Kaplan et al 2010). The intensity change threshold of 30kt/24hours is employed to define RI events since it is nearly 95% percentile of the intensity changes in 24 hours in the WNP (Wang and Zhou 2008; Shu et al. 2012).

The SST, TCHP, VWS between 200 and 850 hPa and RHUM in the 500 hPa are analyzed in order to examine large-scale environment associated with RI. The monthly dataset of the Extended Reconstruction SST (ERSST) is obtained from the National Climatic Data Center (NODC), National Oceanic and Atmospheric Administration (NOAA). The horizontal resolution is 2°×2° (Smith et al. 2008).

Regions where TCHP is more than 60-90 kJ cm^{-2} have been empirically found to be conducive to TC intensification, and TCHP is often used as one of several parameters in hurricane prediction schemes (e.g., DeMaria et al. 2005; Oey et al. 2007). Leipper and Volgenau (1972) developed and formulated TCHP as:

$$TCHP = c_p \int_{D_{26}}^{0} \rho(z)\left[T(z) - 26\right] dz \tag{1}$$

where c_p is specific heat at constant pressure (3.9 kJ kg^{-1} K^{-1}), D_{26} is the depth of 26°C isotherm, $\rho(z)$ is the in-situ density, and $T(z)$ is the in-situ temperature. TCHP is calculated using the monthly mean temperature-salinity from the Simple Ocean Data Assimilation (SODA) which is based on the Parallel Ocean Program ocean model with a horizontal resolution of 0.5°×0.5° and with 40 vertical levels. The SODA velocity fields are used to calculate the SST advection.

Atmospheric variables are taken from twentieth century Reanalysis version 2 (20CRv2) with monthly temporal and 2°×2°spatial resolutions (Compo et al. 2011). VWS is calculated as magnitude of the vector difference between winds at 200 and 850 hPa.

The oceanic and atmospheric variables for the months of May–November are averaged to represent environmental status of the active RI season. They are linearly detrended prior to analysis. The multidecadal variability is obtained through performing a 7-year Gaussian filter to the detrended oceanic and atmospheric variables.

The overlapping bimonthly mean Multivariate ENSO Index (MEI) is obtained from the Climate Diagnostic Center of NOAA. The MEI is constructed based on the six main variables observed in the tropical Pacific, including sea level pressure (SLP), zonal and meridional components of the surface wind, SST, surface air temperature, and total cloudiness fraction of the sky (Wolter and Timlin 1998). The PDO index is constructed using the ERSST from NODC, which is defined as the leading principal component of monthly SST anomalies in the North Pacific poleward of 20°N (Mantua et al. 1997). The MEI and PDO indices during May–November are averaged to represent the status of the ENSO and PDO during the active RI season.

In this study, the effective degrees of freedom in the correlation significance test are estimated from the formula (Quenouille 1952; Medhaug and Furevik 2011; Wang et al. 2012):

$$N_{edf} = \frac{N}{\left(1+2\times r_{x_1}\times r_{y_1}+2\times r_{x_2}\times r_{y_2}\right)} \qquad (2)$$

where N is the length of time series x and y, r_{x_1} and r_{y_1} are the autocorrelations at lag 1, and r_{x_2} and r_{y_2} the autocorrelations at lag two for time series x and y, respectively.

The degrees of freedom in the significance test of mean difference are calculated as (Michael 1986):

$$DF = \frac{\dfrac{\sigma_x^2}{n_x} + \dfrac{\sigma_y^2}{n_y}}{\left\{\left[\dfrac{\sigma_x^2}{n_x\left(n_x - 1\right)}\right] + \left[\dfrac{\sigma_y^2}{n_y\left(n_y - 1\right)}\right]\right\}} \tag{3}$$

where σ_x and σ_y is the standard deviation of the time series *x* and *y*, n_x and n_y is the length of the time series *x* and *y*, respectively. If DF is not an integer, it is rounded off to the nearest integer.

3. RI climatology

Over the WNP from 120°E to 180°E, 1223 RI events occur in 485 TCs of all 1346 TCs (excluding tropical depression) during 1951–2008 (Note that a TC is likely to undergo at least one RI process during its lifecycle). The climatological annual-mean RI number in the WNP is 21.1 with a standard deviation of 14.4. Figure 1 shows climatological monthly variations of the RI and TC numbers in the WNP for the entire period of 1951–2008. The pronounced occurrence of RI events appears during May–November. The maximum number of RI events in the WNP occurs in August and the minimum in February. The maximum (minimum) RI number may be related to more (less) TC genesis in August (February), which increases (decreases) the probability of RI occurrence (Fig. 1b). The number of RI during the months of May–November is 1122, which accounts for about 92% of the total RI number. We therefore focus on the related variation of large-scale environment in the active RI season of May–November in the following sections.

Figure 2 shows the distribution of the 24-h tracks during each RI period as well as the total and annual-mean number of RI cases in each 5×5 box during the period of 1951-2008. RI events tend to be more restricted in the region south of 25°N, with very few cases occurring north of 25°N. The RI events tend to be more concentrated in the area between 8°N–20°N and 125°E–155°E where there is 68% of RI events. This area is defined as the main RI region. The maximum core region locates around 130°E, 15°N and gradually decreases extending eastward to 150°E. The maximum RI number in 5°×5° box reaches about 115 with the annual mean of 2 during 1951–2008. The features showed here are consistent with the results of Shu et al. (2012).

4. Multidecadal variability of RI and large-scale environment

An important source of multidecadal climate variability is the PDO in the North Pacific, which has an ENSO-like spatial signature in the SST field (e.g., Mantua et al. 1997; Zhang et al. 1997). It was found that the PDO has a significant influence on TC activity over the WNP (e.g., Wang et al. 2010; Aiyyer and Thorncroft 2011; Liu and Chan 2013). In this section we attempt to investigate the multidecadal variability of RI and large-scale environment associated with the PDO.

a. Multidecadal variability of RI and its relationship with the PDO

The multidecadal variation in the annual RI number can be obviously seen from its time series (Fig. 3a, b). The RI numbers are above the normal during 1951–1972 and 2002–2008, and below the normal during 1973–2001. Such multidecadal variability of RI is reminiscent to the PDO variations. The PDO shows two cold phase periods: 1951–1978 (period I), 1998–2008 (period III), and a warm phase period: 1979–1997 (period II) (e.g., Shen et al. 2006; Wang et al 2009). There are generally higher values of RI during periods I and III, and lower values during period II. The mean numbers for each of these three sub-periods are 28.5, 9.0, and 23.1 with the standard deviations of 13.7, 5.3, and 13.7, respectively. For the comparison of two cold phases, the annual-average RI number in period I is higher than that in period III, which may be related to more TC genesis in period I. One can clearly see in Figs. 3a,b that the TC number in period I is much higher than that in period III, which increases the chance of RI occurrence in period I.

The standardized time series of the annual RI number and PDO index are displayed in Figs. 3c, d. For the indices including all timescale variations, the correlation between the PDO and RI number is only about -0.11 (Fig. 3c). However, if we focus on longer timescale variation, the relationship between two indices is obvious (Fig. 3d). The correlation reaches about -0.51 with the effective degrees of freedom of 16, which is statistically significant at the 95% confidence level. This suggests a much greater influence of the PDO on the multidecadal variability of RI.

To further clarify the PDO effect, we identify the positive (negative) years of the PDO if the standardized PDO index during May–November is ≥ 0.5 (≤ -0.5). The annual-mean number of RI in the -PDO years (23 years) and the +PDO years (11 years) are 22.9 and 16.9, respectively, and the mean difference is statistically significant at the 95% confidence level. Previous studies have found that ENSO can significantly influence the occurrence of RI in the WNP (e.g., Wang and Zhou 2008). The changes in the RI number may be due to ENSO events rather than the PDO because some +PDO (-PDO) years may be linked with El Niño (La Niña) events (e.g., Liu and Chan 2013). To remove the ENSO effect, we only consider ENSO neutral years (i.e., the average MEI index during May–November is between -0.5 and 0.5). The annual-mean RI number for the -PDO years in ENSO neutral year (1952, 1953, 1961, 1963, 1998, 2000, 2001, 2008) is 22.4, which is much higher than 7 for the +PDO years (1981, 1995, 1996) in ENSO neutral years. The mean difference between them is statistically significant in the 95% confidence level.

The spatial distributions of the RI number and anomaly in each 5°×5° box for each of the three sub-periods (periods I, II and III) are shown in Fig. 4. The RI number anomalies in the three sub-periods are calculated as the RI numbers of the climatological mean over the 1951–2008 subtracted from each of the three sub-periods. Over the most of the main RI region, the climatological mean of the RI number in periods I and III is much higher than that in period II. The maximum cores of the average RI number in periods I and III locate near 130°E, whereas in period II the core shifts eastward to 140°E. It is also clear that the maximum core in period III shifts more northward. In fact, compared with that (15.14°N, 136.44°E) in period II, the average initial positions of the RI occurrence in periods I (15.67°N, 137.95°E) and III (16.33°N, 137.38°E) tend to shift poleward and westward, and the averaged position difference is statistically significant at the 99% confidence level.

b. Large-scale environmental factors related to RI

It has been shown that RI events have significant multidecadal variation associated with the PDO phases. The next part of this study is to identify the possible environmental factors responsible for such variations. The variations of large-scale ocean and atmosphere environmental variables such as SST, TCHP, VWS and RHUM are examined first and their possible relationships with TC RI are then discussed. The potential influence of large-scale environment on TC RI is investigated through composite anomaly in three sub-periods associated with the PDO phases. To compare the differences among the three sub-periods, the SST, TCHP, VWS, and RHUM anomalies are calculated by subtracting the climatological mean for May–November during 1951–2008 from those of the three sub-periods (Figs. 5 and 6). In the main RI region, the region-averaged magnitudes for SST, TCHP, VWS and RHUM are calculated during periods I, II, and III (Table 1).

The distributions of the climatological mean SST for three sub-periods are shown in Fig. 5. The 26°C contour in period II is basically confined to the south of 20°N, whereas in periods I and III it shifts northward and exceeds the latitudinal line of 20°N between about 140°E and 180°E. According to Gray (1979), the TC development is assumed not to be possible if the SSTs are less than 26°C. Thus, the relevant RI events in periods I and III are more occurring in the region north of 20°N than those in period II. The SST anomaly structures in period II associated with the warm PDO phase consist of a tongue of positive SST anomalies stretching from the equatorial central Pacific to the eastern North Pacific, extending along the West Coast of the United States. Negative SST anomalies are found in the tropical western Pacific, extending northeastward to the subtropical latitudes of the central North Pacific. In contrast, the SST anomaly structures in periods I and III associated with the cold PDO phase show an opposite pattern (Fig. 5). In the cold (warm) PDO phase, anomalous warming (cooling) prevails over the main RI region (Fig. 5). The region-averaged SSTs of periods I and III are higher than that of period II in the main RI region. The mean difference between these periods is statistically significant at the 95% confidence level (Table 1). These results suggest that the SST anomaly in the main RI region may potentially contribute to the anti-correlation between the PDO and annual RI number on multidecadal timescales.

The regions where TCHP is more than 60-90 kJ cm^{-2} have been empirically found to be conducive to TC intensification (e.g., Lin et al. 2008). One can note in the distributions of the climatological mean TCHP for each of the three sub-periods that the area surrounded by 60 kJ cm^{-2} contours in period II is much smaller than those in periods I and III over the main RI region. This tends to decrease the probability of RI occurrence in period II. The TCHP anomaly pattern exhibits a distinct east-west dipole in the tropical Pacific with a significantly positive (negative) anomaly in the eastern (western) Pacific in association with the warm (cold) PDO phase (Fig. 5). During periods I and III, the region-averaged TCHPs in the main RI region are 74.51 and 82.61 kJ cm^{-2}, which are higher than 66.64 kJ cm^{-2} of period II. The mean differences between them are statistically significant at the 99% confidence level (Table 1). These results suggest that compared to the warm PDO phase, the ocean in the cold PDO phase may provide more heat energy to the atmosphere over the main RI region, which is favorable to generate TC RI events.

Weak VWS is one of the key environmental factors that promote TC intensification (e.g., Gray 1979; Kaplan and DeMaria et al. 2003; Shu et al. 2012). The VWS in periods I and III is slightly above the climatology mean along the low shear zone that is defined as the area surrounded by the 4 m s^{-1} contours in Fig. 6. Locating in the southwest and northwest flanks of the low shear zone, the VWS anomalies in periods I and III are negative. In contrast, those in period II show an opposite pattern. One can find that RI events in period II less occur in the north of 20°N where the positive VWS anomaly is less conducive for RI (Fig. 6 and Table 2). Therefore, it suggests that variability of the VWS in the southwest and northwest of the low shear zone can be critical for the variability of annual RI number, but it is not in the low shear zone. This is likely due to the reason that VWS is usually below threshold values in the low shear zone for each phase of the PDO. Although the mean VWS differences between periods I, III and II are not statistically significant at the 95% confidence level (Table 1), the average VWS in the main RI region in the periods I and III is still lower than that in period II.

RHUM in the mid-troposphere is one of the key factors influencing TC development, with high values of RHUM being necessary to overcome negative effects of the entrainment on convection during the TC development stage (e.g., Gray 1979, 1988). The thermodynamic factors such as RHUM and SST are not independent, but cooperate to influence instability and potential for cumulonimbus convection (Gray 1979). The RHUM shows similar anomaly pattern to the SST anomaly in some regions. For example, during the warm (cold) PDO phase, positive (negative) RHUM anomalies exist in the tropical eastern Pacific. In contrast, RHUM anomalies in the tropical western Pacific show an opposite sign. The RHUM fields show positive anomaly in the most of the main RI region during periods I and III, especially period III (Fig. 6). Compared with those in period II, RHUMs in periods I and III are above the average in the belt between 20°N and 30°N, and those conditions are more conducive for RI. Actually, this also can result in more occurrences of RI events in the north of 20°N (Fig. 6 and Table 2). While the average RHUM differences between periods I, III and II are not statistically significant at the 95% confidence level (Table 1), mean magnitude of the RHUM in the main RI region in the periods I and III is still higher than that in period II.

Next, in order to further examine relationship between RI and large-scale environmental factors, correlations of the SST, TCHP, VWS and RHUM during May–November with the annual RI number series are calculated (Fig. 7). On multidecadal timescale, the correlation map between the annual RI number and SST shows a PDO-like pattern in the North Pacific. An active (inactive) RI era is associated with a warm (cold) western Pacific and a cold (warm) eastern Pacific. The maximum core of the positive correlation emerges in the region of 10°N–30°N, 160°E–200°E where amplitude of the PDO mode is the strongest (Fig. 7a). The correlation field between TCHP and annual RI number almost exhibits a coherent pattern with the TCHP anomaly fields in Fig. 5, with an east-west seesaw distribution. The annual RI number is positively (negatively) correlated with a warm (cold) tropical western (eastern) Pacific (Fig. 7b).

The correlation map between the VWS and annual RI number is similar to the VWS anomaly pattern in Fig. 6. The positive correlations are found over the tropical eastern Pacific, with maximum magnitude near 10°N, 230°E (Fig. 7c). The significantly negative correlation exists in the belt of 20°N–30°N, which tends to support that more RI events in the cold PDO phase occur in the north of 20°N than in the warm PDO phase (Table 2). The correlation map between the RHUM and annual RI number displays an ENSO-like pattern in the equatorial Pacific, with a positive (negative) correlation in western (eastern) equatorial Pacific. The correlation in most of the western equatorial Pacific is significant at the 95% confidence level (Fig. 7d). The results suggest that a high (low) occurrence era of RI is associated with a RHUM above (below) average in the tropical western Pacific Ocean. In summary, it has been shown that the multidecadal changes in SST, TCHP, VWS and RHUM may contribute to the variations of the annual RI number on multidecadal timescale.

c. Large-scale environment factors correlated with PDO

To further confirm that the multidecadal variability of RI is associated with the PDO, relationship between large-scale environmental factors and the PDO are examined. The correlation maps between the PDO index and SST, TCHP, VWS, 500-hPa RHUM fields for the months of May–November are examined in Fig. 8. The SST-PDO correlation patterns are characterized by a wedge structure in the tropical eastern Pacific and an opposite pattern extending from the tropical western Pacific to the mid-latitude region of the North Pacific Ocean. The correlations are significant at the 95% confidence level. This structure is well-known and resembles the PDO (e.g., Mantua et al. 1997, Zhang et al. 1997). The PDO is negatively correlated with the local SST in the main RI region (Fig. 8a). This means that when the PDO is in its cold phase, there are positive SST anomalies in the main RI region. In contrast, when the PDO is in its warm phase, there are negative SST anomalies in the main RI region. Thus, this supports that a higher (lower) SST is favorable (unfavorable) for RI in the main RI region during the cold (warm) PDO phase. TCHP-PDO correlations in the tropical North Pacific feature a distinct east-west dipole pattern, which is statistically significant at the 95% confidence level. Negative correlations are found over the tropical western Pacific, with the maximum amplitude in the western equatorial Pacific and main RI region. Positive correlations are observed over the tropical eastern Pacific, with the maximum amplitude in the region near 10°N, 210°E (Fig. 8b). This indicates that there are positive (negative) TCHP anomalies in the main RI for the cold (warm) PDO phase. These results further confirm that variation of the oceanic thermodynamic factors such as SST and TCHP over the main RI region may make a contribution to the out-of-phase relationship between the PDO and annual RI number.

The PDO has great influence on the VWS over the tropical Pacific, and subtropical North Pacific. VWS-PDO correlations show a tripole pattern in the south of 40°N. The negative correlation is the strongest within the tropical eastern Pacific and a tongue extends northwestward to near 20°N, 130°E. The significantly positive correlations at the 95% confidence level exist in the western equatorial Pacific and the sector between 20°N and 40°N where the VWS is high (low) in the warm (cold) PDO phase, which tends to suppress (favor) RI occurrence in the region north of 20°N (Fig. 8c and Table 2).

The significantly negative correlations between the RHUM and PDO are found over the western equatorial Pacific, stretching northward to the mid-latitude of the WNP. Negative correlations are statistically significant at the 95% confidence level in the main RI region, which indicates that the RHUM is higher (lower) in the cold (warm) PDO phase. This tends to produce the out-of-phase relationship between the PDO and annual RI number. The significantly positive correlations are observed over the eastern equatorial Pacific, extending northward to the west coast of the United States (Fig. 8d). Overall, the correlation maps between the PDO and environmental factors strongly resemble the corresponding anomaly patterns in Figs. 5 and 6, suggesting that the PDO does make a contribution to their changes which in turn affect the frequency and location of RI events occurrence on multidecadal timescale.

d. Possible physical interpretation

The above analysis using the composites and correlations suggests that the PDO has an association with the multidecadal variability of RI and large-scale environmental factors. It is of importance to understand the mechanism by which the PDO could influence RI and relevant large-scale environment over the main RI region. Vimont et al. (2001, 2003a, b) suggested that during the winter, intrinsic atmospheric variability in the mid-latitudes imparts a SST “footprint” onto the ocean via changes in the net surface heat flux. The SST footprint can persist into the late spring and summer seasons to force an atmospheric circulation anomaly in the region of 0-20°N, which is so-called the seasonal-footprinting-mechanism (SFM). SFM accounts for up to 70% of the inter-decadal variability along the equator (Vimont et al. 2003a). Based on this hypothesis, the relationships between the PDO and thermodynamic factors such as SST, TCHP and RHUM around the main RI region appear to occur due to a link involving surface winds. SLP fields are modified by the preceding winter SST footprint such that the pressure gradient over the equatorial Pacific is changed, resulting in the wind anomaly over these regions. During the warm PDO phase, over the western equatorial Pacific, the SLP increase induces the westerly wind anomalies along the equator (Fig. 9a), which tends to keep the warm water closer to the equator. The reverse is true during the cold PDO phase. This tends to make equatorial warm water spread northward during the cold PDO phase.

TCHP variability mainly involves a link between sea surface wind and oceanic interior. Correlation between PDO and SLP is negative around the center of (15°N, 140°E) (Fig. 9a), which means that there is negative (positive) SLP anomaly in the main RI region for the warm (cold) PDO phase. In turn, the negative (positive) SLP anomaly can induce the cyclonic (anticyclonic) gyre in the warm (cold) PDO phase. Thus, this may shoal (deepen) the D_{26} depth which in turn decreases (increases) the TCHP over the main RI region (Fig. 9b). The Pacific subtropical cells are associated with the divergence of warmer Ekman flows out of the equatorial Pacific forced by the easterly wind (Feng et al. 2010). Thus, the westerly (easterly) wind anomaly during the warm (cold) PDO phase can produce a convergence (divergence) anomaly of the warm equatorial water, which also tends to decrease (increase) TCHP over the main RI region.

The time series of SST, meridional SST advection and the PDO index further support these links (Fig. 10). Examining SST advection between 0-8°N and 125°E-160°E indicates that the regional-averaged meridional SST advection is positively correlated with the averaged-SST in the main RI region. The correlation coefficient is 0.45 which is statistically significant at the 95% confidence level with the effective degrees of freedom of 19. This suggests that SSTs are higher over the main RI region when meridional advection anomalies in the western equatorial Pacific are northward. The correlation between the PDO index and averaged meridional SST advection shows a magnitude of -0.48 which is statistically significant at the 95% confidence level. These relationships offer qualitative support that the warmer water from the western equatorial Pacific tends to spread northward during the cold PDO phase, which may maintain the warm ocean anomaly over the main RI region.

In order to determine the effect of the PDO on VWS, the winds at 850 hPa and 200 hPa are correlated onto the PDO index (Fig. 11). It is clear in the correlation maps that the cold PDO phase is associated with the easterly (westerly) wind anomaly in the lower (upper) troposphere along the equator, which reduces the local VWS in the tropical Pacific. When PDO is in its warm (cold) phase, the westerly (easterly) wind anomalies at lower troposphere level along the equator are attributed to weaker (stronger) than the normal lower-level easterly wind while the upper-level easterly (westerly) wind anomalies in that same region are due to stronger (weaker) than normal upper-level easterly wind (not shown). Simultaneously, the upper troposphere across the belt of 20-50°N is associated with an anticyclonic wind anomaly pattern, which tends to weaken the local VWS to favor RI formation. These results are coherent with the VWS anomaly distribution in Fig. 6. One potential explanation about these features can give based on the Gill's (1980) theory. Gill (1980) show that an equatorial diabatic cooling source can produce anomalous low-level easterlies to its west with the anticyclonic circulations on its northwestern flank as a result of the equatorial Rossby wave response. During the cold PDO phase, the anomalous cooling in the eastern equatorial Pacific may therefore induce the anomalous tropical easterlies at the low level. This therefore can enhance the Walker circulation in the western equatorial Pacific and in turn induce the westerly wind anomaly in the upper level.

5. Summary and discussion

In this paper, we investigate the multidecadal variability of RI and explore how the multidecadal variations of large-scale environmental factors affect the frequency and location of RI events in the WNP. In particular, we focus on the PDO effect on the large-scale environmental factors associated with RI.

The PDO index exhibits significant negative correlation with the annual RI number on multidecadal timescale. The warm (cold) PDO phase is related to the low (high) annual RI number over the WNP. The RI formation tends to shift poleward and westward during the cold PDO phase, while it tends to shift equatorward and eastward during the warm PDO phase.

The analyses show that the multidecadal variations of RI are significantly associated with the variations of large-scale oceanic and atmospheric variables such as SST, TCHP, VWS and RHUM. The SST anomaly patterns in the three sub-periods (1951-1978, 1979-1997, 1998-2008) are strongly similar to the PDO SST mode seen in the global SST field analysis (Zhang et al. 1997). In the cold (warm) PDO phase, anomalous warming (cooling) prevails over the main RI region. A distinct east-west dipole pattern in the TCHP anomaly is identified with significantly positive (negative) anomaly in the western (eastern) Pacific, which is in association with the cold (warm) PDO phase. RHUM anomaly shows a similar pattern to SST anomaly over the WNP, suggesting the cooperating influence of RHUM and SST on RI. The multidecadal variations of the thermodynamic factors are relevant to more (less) occurrence of the RI events in the cold (warm) PDO phase. They thus contribute to the out-of-phase relationship between the PDO and annual RI number on multidecadal timescale.

It is interesting to note that during the cold (warm) PDO phase, the VWS anomaly in the low shear zone (i.e., the climatological average VWS is less than 4 m s^{-1}) is positive (negative), showing an unfavorable (favorable) condition for RI. This suggests that the VWS variation in the low shear zone along the monsoon trough may have little contribution to the anti-correlation between the PDO and annual RI number. However, there are the out-of-phase VWS anomaly patterns in the southwest and northwest flanks of the low shear zone. Thus, variability of the VWS in the southwest and northwest of the low shear zone may be critical for modulation of RI frequency, but it is not in the low shear zone. It is likely that VWS is usually below the RI threshold value in the low shear zone for each phase of the PDO.

It is further confirmed that the multidecadal variability of the SST, TCHP, VWS and RHUM during the active RI season is significantly correlated with the PDO. On multidecadal timescale, correlations between the PDO and SST over the mid-latitude of the WNP is up to -0.9, which affects SLP pattern as well as the winds and then affects ocean interior. The correlation maps between the PDO and environmental factors such as

SST, TCHP, VWS and RHUM strongly resemble the individual anomaly patterns associated with the PDO phases, suggesting that the PDO makes a contribution to the changes which in turn affect the RI variability on multidecadal timescale.

The mechanisms by which the PDO affects large-scale oceanic and atmospheric environment over the main RI region are inferred from the SFM hypothesis (Vimont et al. 2001, 2003a, b). In the active RI season, the SLP fields are modified by the preceding winter SST footprint such that the pressure gradient between the western equatorial Pacific and eastern equatorial Pacific is changed, resulting in the wind anomaly over the equatorial region. During the cold PDO phase, over the western (eastern) equatorial Pacific, the SLP decrease (increase) induces the easterly wind anomaly in the low level along the equator. Hence, the Walker circulation can be enhanced to induce a westerly wind anomaly in the upper level. The anomalous easterly wind further may produce local equatorial ocean upwelling to diverge the warmer water northward from the western equatorial Pacific into the main RI region, which in turn maintains the warm ocean anomalies over the main RI region. Simultaneously, the area of high mid-tropospheric RHUM associated with the warmer water spreads from the western equatorial Pacific into the main RI region. Our analysis also shows that the cold PDO phase can induce a local anticyclonic wind anomaly in the subtropical gyre of the WNP. This therefore may deepen D_{26} and directly increase the TCHP over the main RI region. These thermodynamic effects during the cold PDO phase greatly support RI occurrence over the WNP. The situation is the opposite during the warm PDO phase.

This study suggests a new mechanism by which the PDO may modulate large-scale environmental factors to make a contribution to TC RI over the WNP on multidecadal timescale. Coupled variability of the North Pacific SST and the atmosphere involves the complex thermodynamic/dynamic processes. There may be other mechanisms for the link between the North Pacific SSTs and atmospheric variability. But, it is beyond the scope of this study to discuss them. Alexander (2010) provides a detailed review and discussion on this topic.

Acknowledgements

This study is supported by the National Basic Research Program of China (2013CB430304 and 2013CB430301), National Natural Science Foundation (41030854, 41106005, 41176003, 41206178, 41376015 and 41306006) of China, and National High-Tech R&D Program (2013AA09A505) of China. Xidong Wang is also supported by China Scholarship Council.

References

Aiyyer, A., and C. Thorncroft, 2011: Interannual-to-multidecadal variability of vertical shear and tropical cyclone activity. *J. Clim.*, **24**, 2949–2962.

Alexander, M. A., 2010: Extratropical Air-Sea Interaction, SST Variability and the Pacific Decadal Oscillation (PDO). *Climate Dynamics: Why does Climate Vary*, Editors D. Sun and F. Bryan, AGU Monograph #189, Washington D. C., 123-148.

Ali, M. M., P. S. V. Jagadeesh, and S. Jain, 2007: Effects of eddies on Bay of Bengal cyclone intensity. *EOS Trans Amer Geophys Union*, **88**: 93–95.

Balaguru, K., P. Chang, R. Saravanan, L. R. Leung, Z. Xu, M. K. Li, and J. S. Hsieh, 2012: Ocean barrier layers' effect on tropical cyclone intensification. *PNAS*., doi:10.1073/pnas.1201364109.

Bender, M. A., and I. Ginis, 2000: Real-case simulations of hurricane–ocean interaction using a highresolution coupled model: effects on hurricane intensity. *Mon. Wea. Rev.*, **128**, 917–946.

Chan, J. C. L., Y. H. Duan, and L. K. Shay, 2001: Tropical cyclone intensity change from a simple ocean–atmosphere coupled model. *J. Atmos. Sci.*, **58**, 154–172.

Chan, J. C. L., 2006: Comment on "Changes in tropical cyclone number, duration, and intensity in a warming environment". *Science*, **311**, 1713.

Chan, J. C. L., 2008: Decadal variations of intense typhoon occurrence in the western North Pacific. *Proc. R. Soc. A.*, **464**, 249–272.

Chen, H., D. L. Zhang, J. Carton, and R. Atlas, 2011: On the rapid intensification of Hurricane Wilma (2005), Part I: Model prediction and structural changes. *Wea. Forecasting*, **26**, 885-901.

Cione, J. J., and E. W. Uhlhorn, 2003: Sea Surface Temperature Variability in Hurricanes: Implications with Respect to Intensity Change. *Mon. Wea. Rev.*, **131**, 1783–1795.

Compo, G. P. et al., 2011: The twentieth century reanalysis project. *Q. J. R. Meteorol. Soc.*, **137**, 1–28.

DeMaria, M., M. Mainelli, L. K. Shay, J. A. Knaff, and J. Kaplan, 2005: Further improvements to the statistical hurricane intensity prediction scheme (SHIPS). *Wea. Forecasting*, **20**, 531–543.

DeMaria, M., C. R. Sampson, J. A. Knaff, and K. D. Musgrave, 2014: Is tropical cyclone intensity guidance improving? *Bull. Am. Meteorol. Soc.*,DOI:10.1175/BAMS-D-12-00240.I

Elsberry, R., T. D. B. Lambert, and M. A. Boothe, 2007: Accuracy of Atlantic and eastern North Pacific tropical cyclone intensity forecast guidance. *Wea. Forecasting*, **22**, 747-762.

Emanuel, K. A., 1999: Thermodynamic control of hurricane intensity. *Nature*, **401**, 665–669.

Emanuel, K. A., C. DesAutels, C. Holloway, and R. Korty, 2004: Environmental control of tropical cyclone intensity. *J. Atmos. Sci.*, **61**, 843–858.

Emanuel, K. A., 2005: Increasing destructiveness of tropical cyclones over the past 30 years. *Nature*, **436**, 686–688.

Gill, A. E., 1980: Some simple solutions for heat-induced tropical circulation. *Quart. J. Roy. Meteor. Soc.*, **106**, 447–462.

Goni, G., M. DeMaria, J. Knaff , C. Sampson, I. Ginis, F. Bringas, A. Mavume, C. Lauer, I-I Lin, M. M. Ali, P. Sandery, S. Ramos-Buarque, K. Kang, A. Mehra, E. Chassignet, and G. Halliwell, 2009: Applications of satellite-derived ocean measurements to tropical cyclone intensity forecasting. *Oceanography*, **22(3)**, 190–197.

Gray, W. M., 1979: Hurricanes: Their formation, structure and likely role in the tropical circulation. *Meteorology over the Tropical Oceans*, D. B. Shaw, Ed., Royal Meteorological Society, 155–218.

Gray, W. M., 1988: Environmental influences on tropical cyclones. *Aust. Meteor. Mag.*, **36**, 127–139.

Ho, C. H., J. J. Baik, J. H. Kim, D. Y. Gong, and C. H. Sui, 2004: Interdecadal changes in summertime typhoon tracks. *J. Clim.*, **17**, 1767–1776.

Kaplan, J., and M. DeMaria, 2003: Large-scale characteristics of rapidly intensifying tropical cyclones in the north Atlantic basin. *Wea. Forecasting*, **18**, 1093–1108.

Kaplan, J., M. DeMaria, and J.A. Knaff, 2010: A revised tropical cyclone rapid intensification index for the Atlantic and East Pacific basins. *Wea. Forecasting*, **25**, 220–241.

Landsea, C. W., 2005: Hurricanes and global warming. *Nature*, **438**, E11–E12. doi:10.1038/nature04477

Leipper, D., 1967: Observed ocean conditions and Hurricane Hilda, 1964. *J. Atmos. Sci.*, **24**, 182–196.

Leipper, D., and D. Volgenau, 1972: Hurricane heat potential of the Gulf of Mexico. *J. Phys. Oceanogr.*, **2**, 218–224.

Lin, I-I, C. C. Wu, K. Emanuel, I. H. Lee, C. R. Wu, and I. F. Pun, 2005: The interaction of Supertyphoon Maemi (2003) with a warm ocean eddy. *Mon. Wea. Rev.*, **133(9)**, 2635–2649.

Lin, I-I, C. C. Wu , I. F. Pun, and D. S. Ko, 2008: Upper-ocean thermal structure and the western North Pacific category 5 typhoons. Part I: ocean features and the category 5 typhoons' intensification. *Mon. Wea. Rev.*, **136(9)**, 3288–3306.

Lin, I-I, C. H. Chen, I. F. Pun, W. T. Liu, and C. C. Wu, 2009a: Warm ocean anomaly, air sea fluxes, and the rapid intensification of tropical cyclone Nargis (2008). *Geophys. Res. Lett.*, **36**, L03817.

Lin, I-I, I. F. Pun, and C. C. Wu, 2009b: Upper ocean thermal structure and the western North Pacific category-5 typhoons part II: dependence on translation speed. *Mon. Wea. Rev.*, **137(11)**, 3744–3757.

Liu, K. S., and J. L. C. Chan, 2013: Inactive period of Western North Pacific tropical cyclone activity in 1998-2011. *J. Clim.*, **26(8)**, 2614–2630.

Mainelli, M., M. DeMaria, L. K. Shay, and G. Goni, 2008: Application of oceanic heat content estimation to operational forecasting of recent Atlantic category 5 hurricanes. *Wea. Forecasting*, **23**, 3–16.

Mantua, N. J., S. R. Hare, Y. Zhang, J. M.Wallace, and C. R. Francis, 1997: A Pacific interdecadal climate oscillation with impacts on salmon production. *Bull. Am. Meteorol. Soc.*, **78(6)**, 1069–1079.

Medhaug, I., and T. Furevik, 2011: North Atlantic 20th century multidecadal variability in coupled climate models: Sea surface temperature and ocean overturning circulation. *Ocean Sci.*, **7**, 389–404.

Michael, O. M., 1986: *Sensory Evaluation of Food: Statistical Methods and Procedures*. CRC Press, 487PP. ISBN0-8247-7337-3.

Oey, L. Y., T. Ezer, D. P. Wang, X. Q. Yin, and S. J. Fan, 2007: Hurricane-induced motions and interaction with ocean currents. *Cont. Shelf. Res.*, **27**, 1249–1263.

Quenouille, M. H., 1952: *Associated Measurements*. Butterworths Scientific Publications, 242 pp.

Rappaport, E. N., and Coauthors, 2009: Advances and challenges at the National Hurricane Center. *Wea. Forecasting*, **24**, 395–419.

Rozoff, C. M., and J. P. Kossin, 2011: New probabilistic forecast models for the prediction of tropical cyclone rapid intensification. *Wea. Forecasting*, **26(5)**, 677-689.

Schade, L. R., and K. A. Emanuel, 1999: The ocean's effect on the intensity of tropical cyclones: results from a simple coupled atmosphere–ocean model. *J. Atmos. Sci.*, **56**, 642–651.

Shen, C. M., W. C. Wang, W. Gong, and Z. X. Hao, 2006: A Pacific Decadal Oscillation record since 1470 AD reconstructed from proxy data of summer rainfall over eastern China. *Geophys. Res. Lett.*, Doi:10.1029/2005GL024804.

Shay, L. K., G. J. Goni, and P. G. Black, 2000: Effects of a warm oceanic feature on Hurricane Opal. *Mon. Wea. Rev.*, **128**, 1366–1383.

Shu, S. J., J. Ming, and P. Chi, 2012: Large-scale characteristics and probability of rapidly intensifying tropical cyclones in the western north pacific basin. *Wea. Forecasting*, **27**, 411–423.

Smith, T. M., R. W. Reynolds, T. C. Peterson, and J. Lawrimore, 2008: Improvements to NOAA's Historical Merged Land-Ocean Surface Temperature Analysis (1880-2006). *J. Clim.*, **21**, 2283–2296.

Ventham, J. D., and B. Wang, 2007: Large scale flow patterns and their influence on the intensification rates of western north Pacific tropical stroms. *Mon. Wea. Rev.*, **135**: 1110–1127.

Vimont, D. J., D. S. Battisti, and A. C. Hirst, 2001: Footprinting: A seasonal connection between the tropics and midlatitudes. *Geophys. Res. Lett.*, **28**, 3923–3926.

Vimont, D. J., D. S. Battisti, and A. C. Hirst, 2003a: The seasonal footprinting mechanism in the CSIRO general circulation models. *J. Clim.*, **16**, 2653–2667.

Vimont, D. J., J. M. Wallace, and D. S. Battisti, 2003b: The seasonal footprinting mechanism in the Pacific: Implications for ENSO. *J. Clim.*, **16**, 2668–2675.

Wang, B., and X. Zhou, 2008: Climate variation and prediction of rapid intensification in tropical cyclones in the western North Pacific. *Meteorol. Atmos. Phys.*, **99**, 1–16.

Wang, B, Y. Yang, Q. H. Ding, H. Murakami, and F. Huang, 2010: Climate control of the global tropical storm days (1965–2008). *Geophys. Res. Lett.*, doi:10.1029/2010GL042487.

Wang, C. Z., S. F. Dong, A. T. Evan, G. R. Foltz, and S-K Lee, 2012: Multidecadal Covariability of North Atlantic Sea Surface Temperature, African Dust, Sahel Rainfall, and Atlantic Hurricanes. *J. Clim.*, **25**, 5404–5405.

Wang, X. D., G. J. Han, Y. Q. Qi, and W. Li, 2011: Impact of barrier layer on typhoon-induced sea surface cooling. *Dyn. Atmos. Oceans*, **52**, 367–385.

Wang, X., D. X. Wang, and W. Zhou, 2009: Decadal variability of twentieth-century El Niño and La Niña occurrence from observations and IPCC AR4 coupled models. *Geophys. Res. Lett.*, Doi: 10.1029/2009GL037929.

Wolter, K., and M. S. Timlin, 1998: Measuring the strength of ENSO events: How does 1997/98 rank? *Weather*, **53**, 315–324.

Yeh, S. W., S. K. Kang, B. P. Kirtman, J. H. Kim, M. H. Kwon, and C. H. Kim, 2010: Decadal change in relationship between western North Pacific tropical cyclone frequency and the tropical Pacific SST. *Meteor. Atmos. Phys.*, **106**, 179–189.

Zhang, Y., J. M. Wallace, and D. S. Battisti, 1997: ENSO-like Interdecadal Variability: 1900-93. *J. Clim.*, **10**, 1004–1020.

Figure captions

Figure 1. Monthly number of (a) RI events and (b) TC genesis (excluding the tropical depression).

Figure 2. (a) 24-h tracks of RI events and the red dots represent the initial location. (b) Total RI number in each 5×5° box during 1951–2008. (c) Annual-mean number in each 5×5° box during 1951–2008.

Figure 3. Time series of (a) the annual RI and TC numbers (excluding the tropical depression), (b) RI and TC anomalies, (c) total standardized RI and PDO index, and (d) filtered standardized RI and PDO index during 1951–2008. A 7-year Gaussian filter is performed to obtain multidecadal variability of the standardized RI and PDO index in the (d).

Figure 4. (a) Climatological mean of the RI number (left panel) and RI number anomaly (right panel) in each 5×5° box over the 1951–1978 (period I). The anomaly is relative to the climatological mean over the 1951–2008. (b) The same as in (a) except for the 1979–1997 (period II). (c) The same as in (a) except for the 1998–2008 (period III). The rectangle box indicates the main RI region.

Figure 5. (a) Climatological mean SST (contour) and SST anomaly (shaded) for each in the three sub-periods. Upper panel: 1951–1978 (period I); Middle panel: 1979–1997 (II period); Lower panel: 1998–2008 (period III). (b) The same as in (a) except for the TCHP.

The SST and TCHP anomalies are calculated by subtracting climatological mean for May–November during1951–2008 from those of the three sub-periods. SST and TCHP are detrended prior to the analysis. The dots show the initial location of RI events and the rectangle box indicates the main RI region.

Figure 6. (a) Climatological mean VWS (contour; Dark brown lines indicate 4m/s VWS contour) and VWS anomaly (shaded) for each of the three sub-periods. Upper panel: 1951–1978 (period I); Middle panel: 1979–1997 (period II); Lower panel: 1998–2008 (period III). (b) The same as in (a) except for the RHUM. VWS and RHUM anomalies are calculated by subtracting climatological mean for May–November during 1951–2008 from those of the three sub-periods. VWS and RHUM are detrended prior to the analysis. The dots show the initial location of RI cases and the rectangle box indicates the main RI region.

Figure 7. Multidecadal correlation maps between the time series of annual RI number and environmental variables (a) SST, (b) TCHP, (c) VWS, and (d) RHUM. The cross sign indicates the statistical significance at the 95% confidence level. Multidecadal variability is obtained to perform a 7-year Gaussian filter to the detrended SST, TCHP, VWS and RHUM fields during May–November. The rectangle box indicates the main RI region.

Figure 8. Multidecadal correlation maps between the PDO index and environmental variables (a) SST, (b) TCHP, (c) VWS, and (d) RHUM. The cross sign indicates the

statistical significance at the 95% confidence level. Multidecadal variability is obtained to perform a 7-year Gaussian filter to the detrended SST, TCHP, VWS, RHUM fields and the PDO index during May–November. The rectangle box indicates the main RI region.

Figure 9. Multidecadal correlation maps between the PDO index and (a) SLP (shaded), 10-m wind (vectors) and (b) D_{26} (shaded), 10-m wind stresses (vectors) during May–November. The cross sign indicates the statistical significance at the 95% confidence level for SLP and D_{26}. The black vectors are statistically significant at the 95% confidence level for wind and wind stress. All variables are smoothed to obtain multidecadal variability by a 7-year Gaussian filter.

Figure 10. Standardized time series of the region-average SST in the main RI region (8°N–20°N, 125°E–155°E), region-average SST meridional advection in the region of 0–8°N and 125°E–160°E, and PDO index during May–November. Each for the three variables is smoothed to obtain the multidecadal variability by a 7-year Gaussian filter.

Figure 11. Correlation maps of (a) 200 hPa wind vectors and (b) 850 hPa wind vectors with respect to the PDO index during May–November. The black vectors are statistically significant at the 95% confidence level. All variables are smoothed to obtain multidecadal variability by a 7-year Gaussian filter.

Table 1. The region-averaged magnitude for SST, TCHP, VWS and RHUM during 1951–1978 (period I), 1979–1997 (period II), and 1998–2008 (period III) in the main RI region. D_1 denotes the difference between periods I and II, and D_2 shows the difference between periods III and I, respectively.

Variable	Unit	Period I	Period II	Period III	D_1=I-II	D_2=III-II
SST	°C	27.19	27	27.41	0.19*	0.41*
TCHP	kJ cm^{-2}	74.51	66.64	82.61	7.87**	15.97**
VWS	m s^{-1}	5.66	5.92	5.55	-0.26	-0.37
RHUM	%	54	53.53	53.81	0.47	0.28

* The difference from the results of a Student t-test is statistically significant at the 95% confidence level.

** The difference from the results of a Student t-test is statistically significant at the 99% confidence level.

Table 2. Annual-averaged RI number in the region north of 20°N, 8°N-20°N and South of 8°N for the PDO cold and warm phase. The number in the bracket indicates total number in the different periods.

PDO phase	North of 20°N	8°N-20°N	South of 8°N
Cold phase(1951-1978)	4.85 (136)	22 (616)	1.6 (46)
Warm phase(1979-1997)	0.94 (18)	8.1 (154)	0 (0)
Cold phase(1998-2008)	7.09 (78)	15.2 (168)	0.72

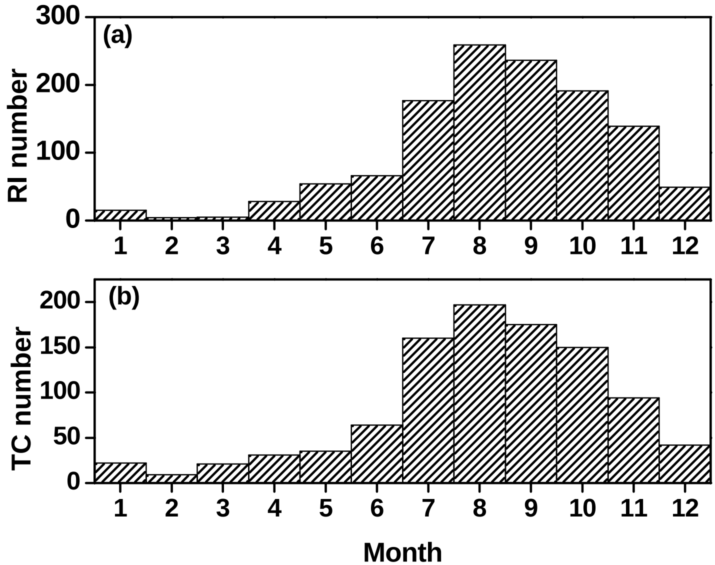

Figure 1. Monthly number of (a) RI events and (b) TC genesis (excluding the tropical depression).

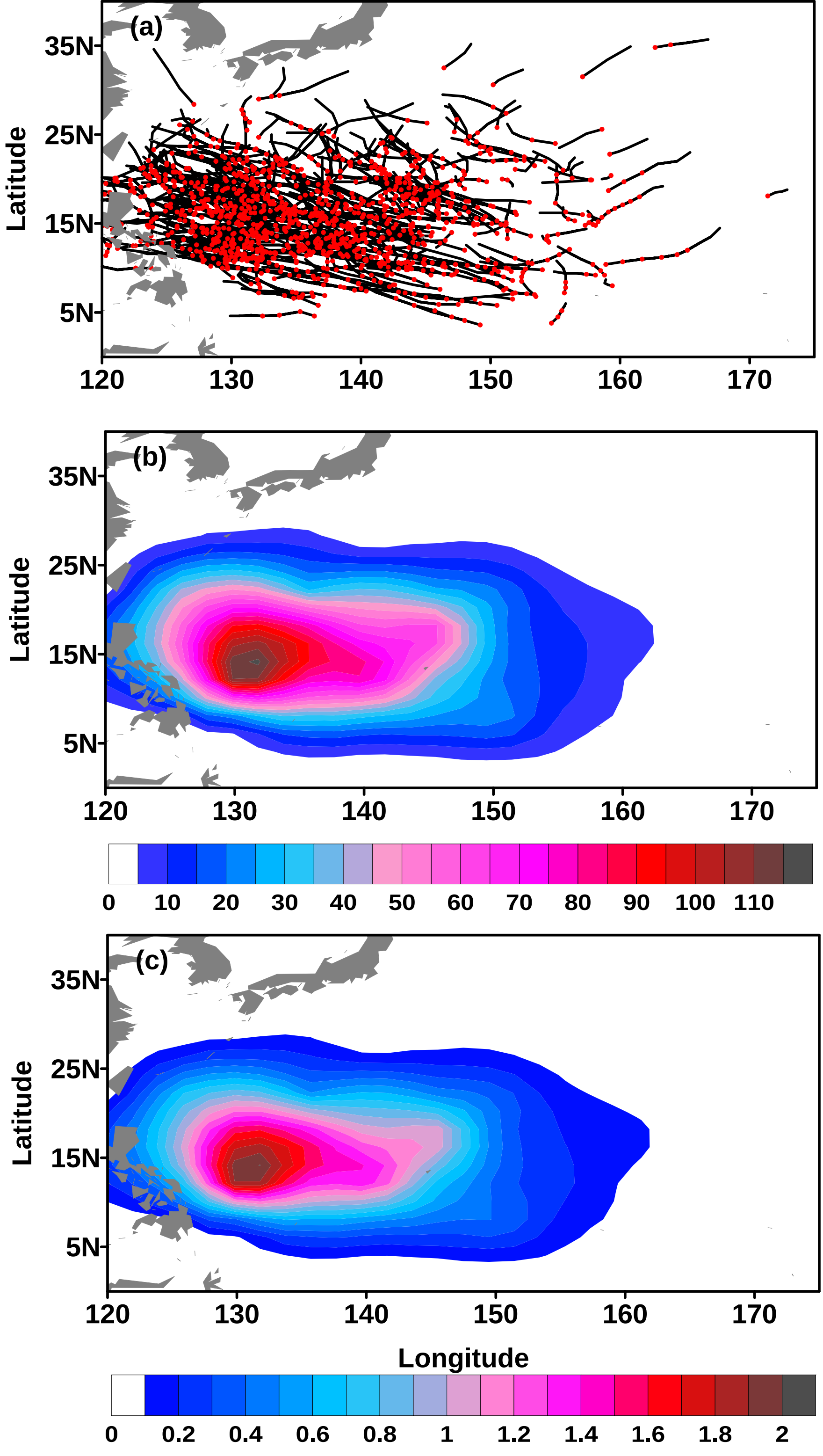

Figure 2. (a) 24-h tracks of RI events and the red dots represent the initial location. (b) Total RI number in each 5×5° box during 1951–2008. (c) Annual-mean number in each 5×5° box during 1951–2008.

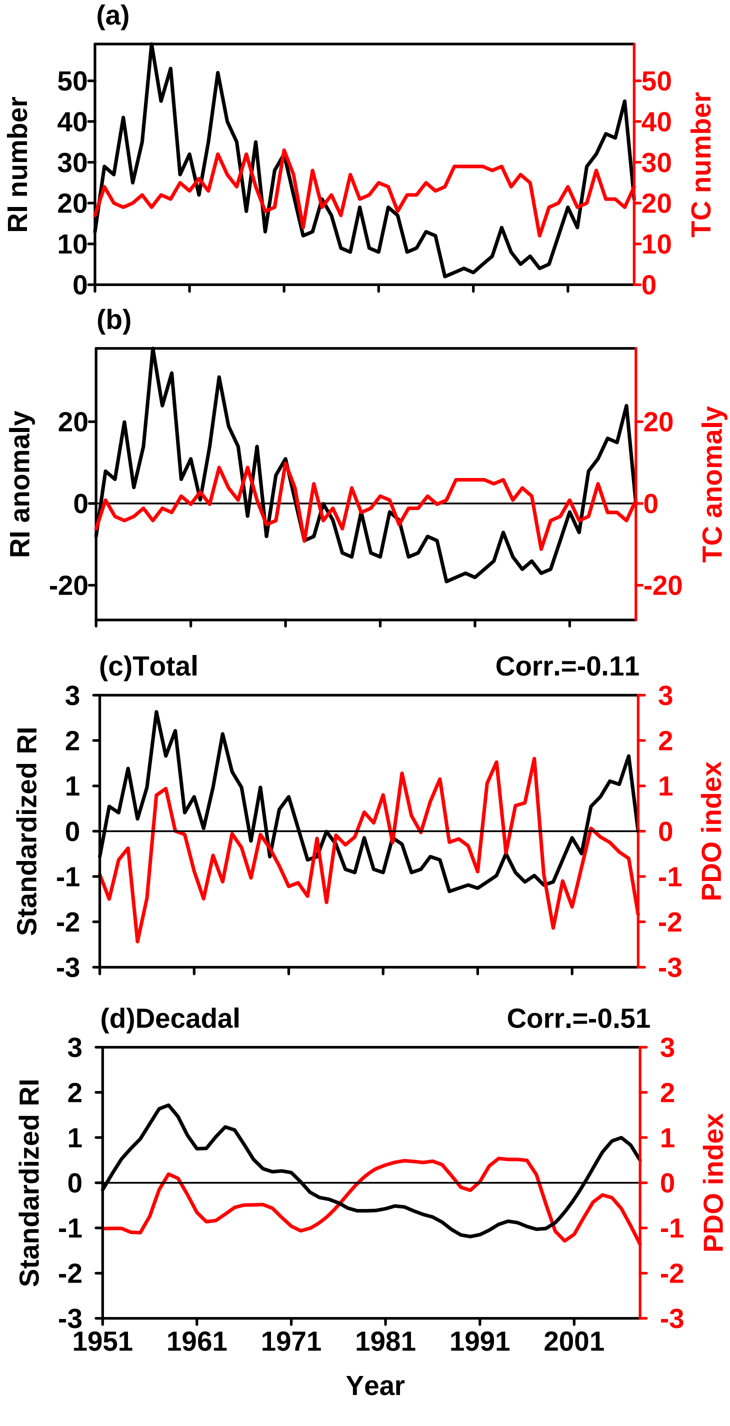

Figure 3. Time series of (a) the annual RI and TC numbers (excluding the tropical depression), (b) RI and TC anomalies, (c) total standardized RI and PDO index, and (d) filtered standardized RI and PDO index during 1951–2008. A 7-year Gaussian filter is performed to obtain multidecadal variability of the standardized RI and PDO index in the (d).

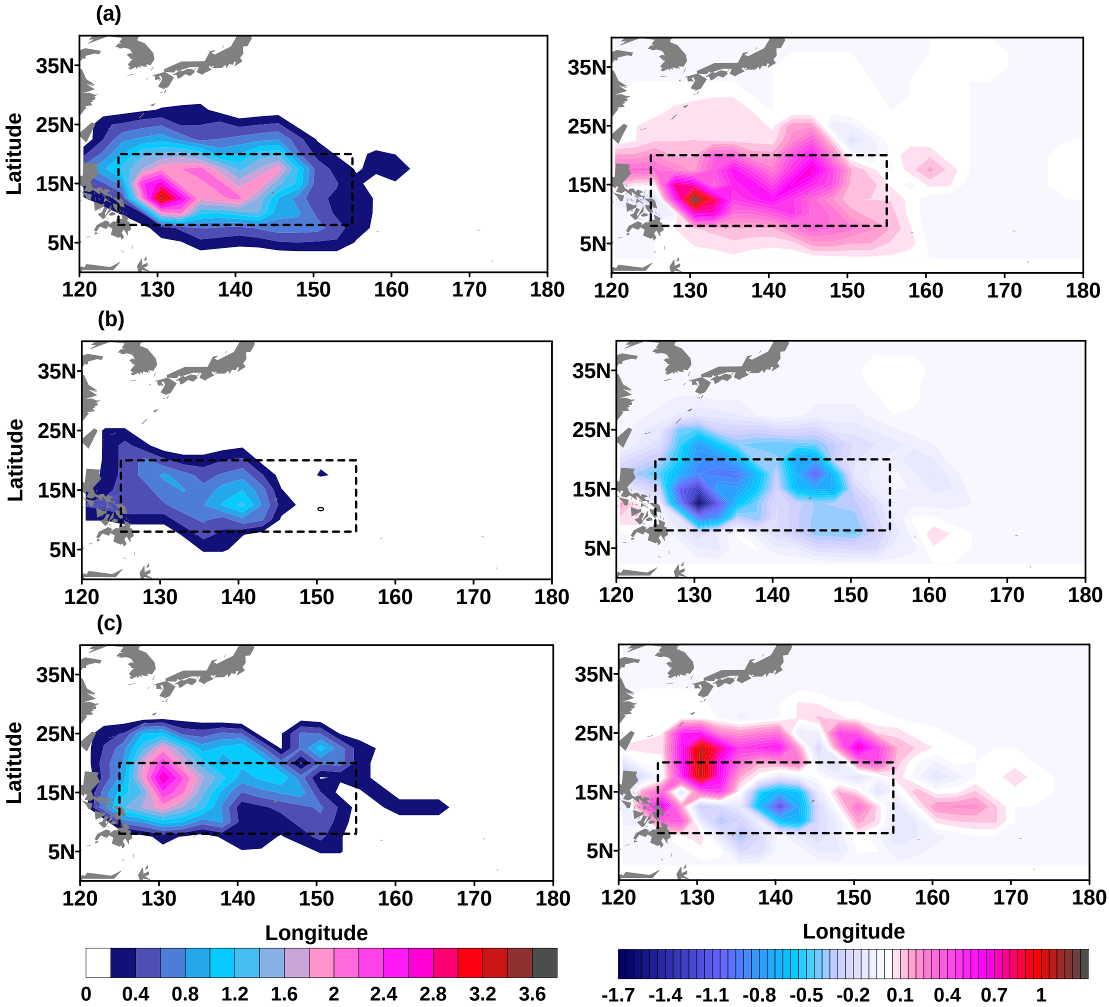

Figure 4. (a) Climatological mean of the RI number (left panel) and RI number anomaly (right panel) in each 5×5° box over the 1951–1978 (period I). The anomaly is relative to the climatological mean over the 1951–2008. (b) The same as in (a) except for the 1979–1997 (period II). (c) The same as in (a) except for the 1998–2008 (period III). The rectangle box indicates the main RI region.

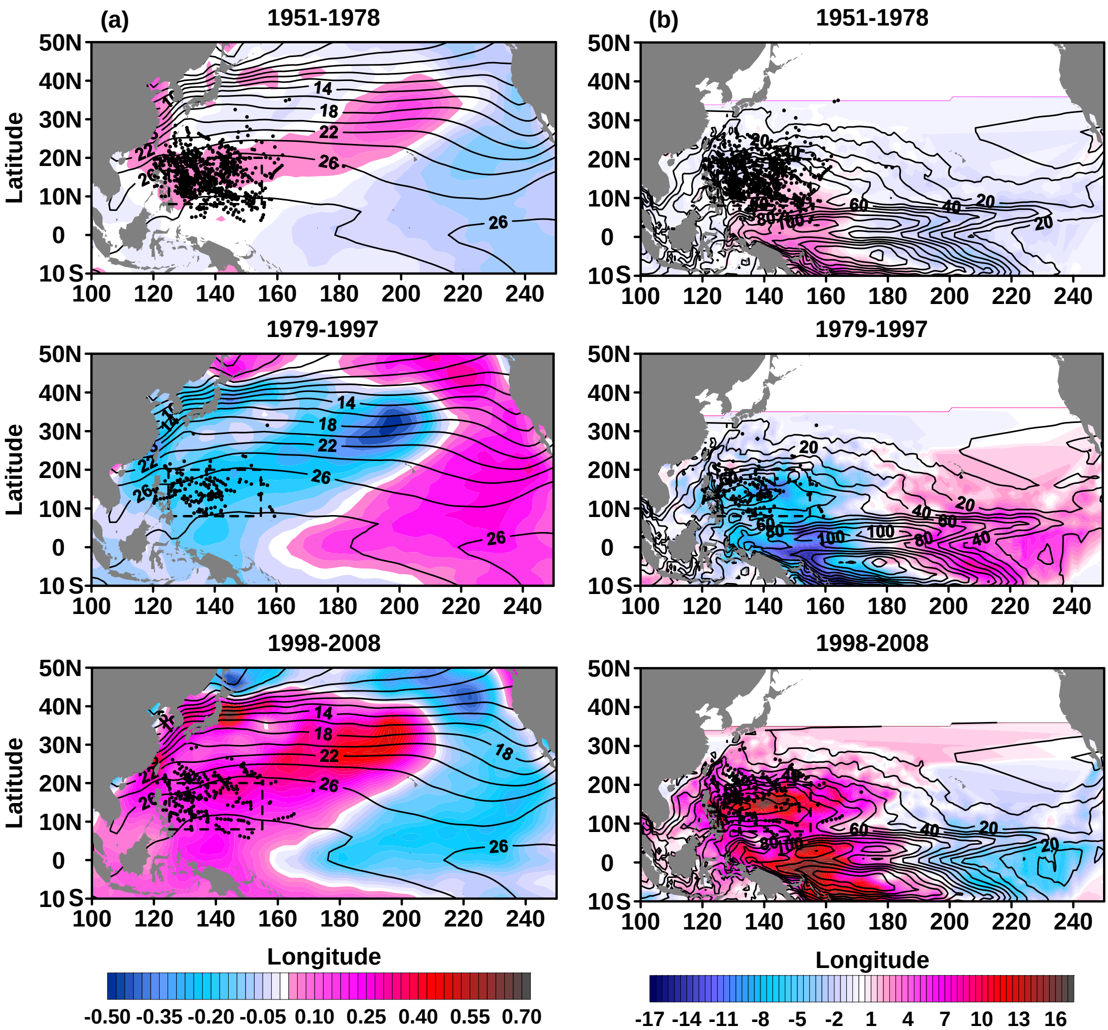

Figure 5. (a) Climatological mean SST (contour) and SST anomaly (shaded) for each in the three sub-periods. Upper panel: 1951–1978 (period I); Middle panel: 1979–1997 (II period); Lower panel: 1998–2008 (period III). (b) The same as in (a) except for the TCHP. The SST and TCHP anomalies are calculated by subtracting climatological mean for May–November during1951–2008 from those of the three sub-periods. SST and TCHP are detrended prior to the analysis. The dots show the initial location of RI events and the rectangle box indicates the main RI region.

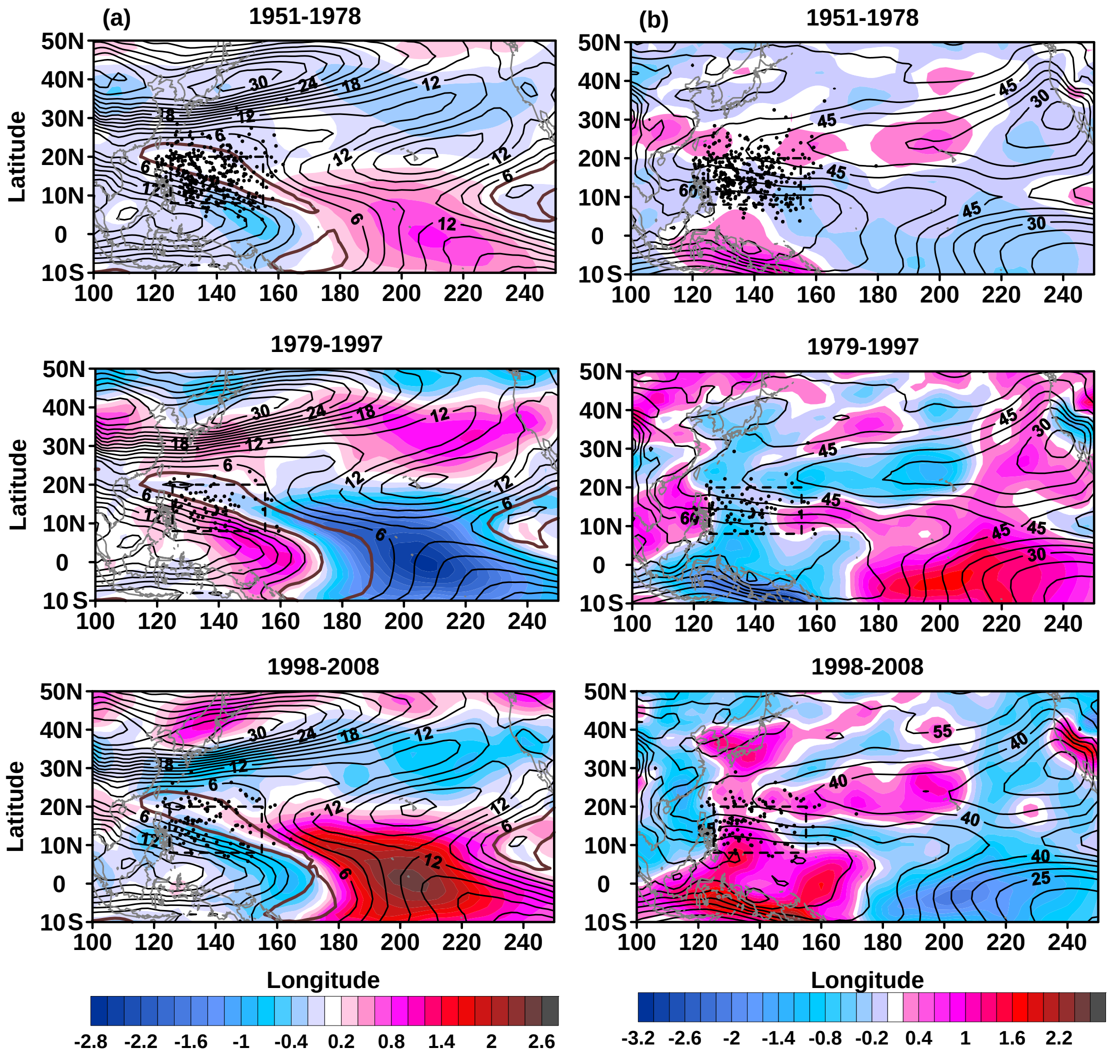

Figure 6. (a) Climatological mean VWS (contour; Dark Brown lines indicate 4m/s VWS contour) and VWS anomaly (shaded) for each of the three sub-periods. Upper panel: 1951–1978 (period I); Middle panel: 1979–1997 (period II); Lower panel: 1998–2008 (period III). (b) The same as in (a) except for the RHUM. VWS and RHUM anomalies are calculated by subtracting climatological mean for May–November during 1951–2008 from those of the three sub-periods. VWS and RHUM are detrended prior to the analysis. The dots show the initial location of RI cases and the rectangle box indicates the main RI region.

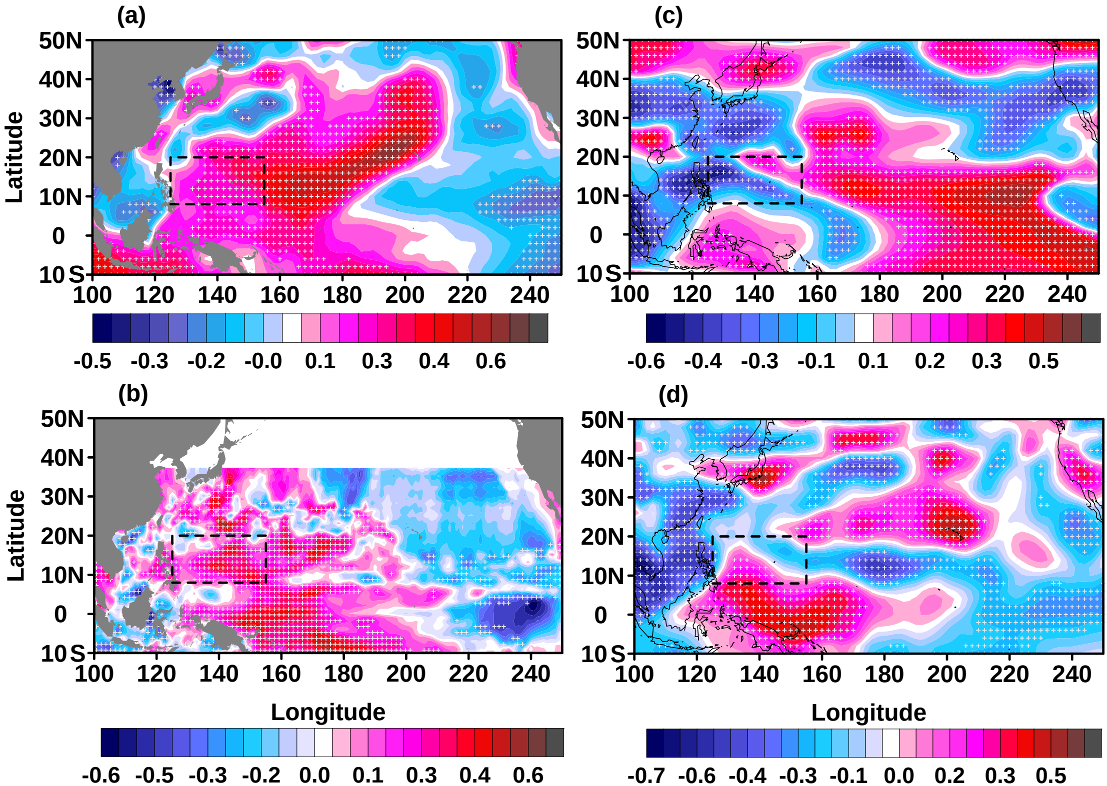

Figure 7. Multidecadal correlation maps between the time series of annual RI number and environmental variables (a) SST, (b) TCHP, (c) VWS, and (d) RHUM. The cross sign indicates the statistical significance at the 95% confidence level. Multidecadal variability is obtained to perform a 7-year Gaussian filter to the detrended SST, TCHP, VWS and RHUM fields during May–November. The rectangle box indicates the main RI region.

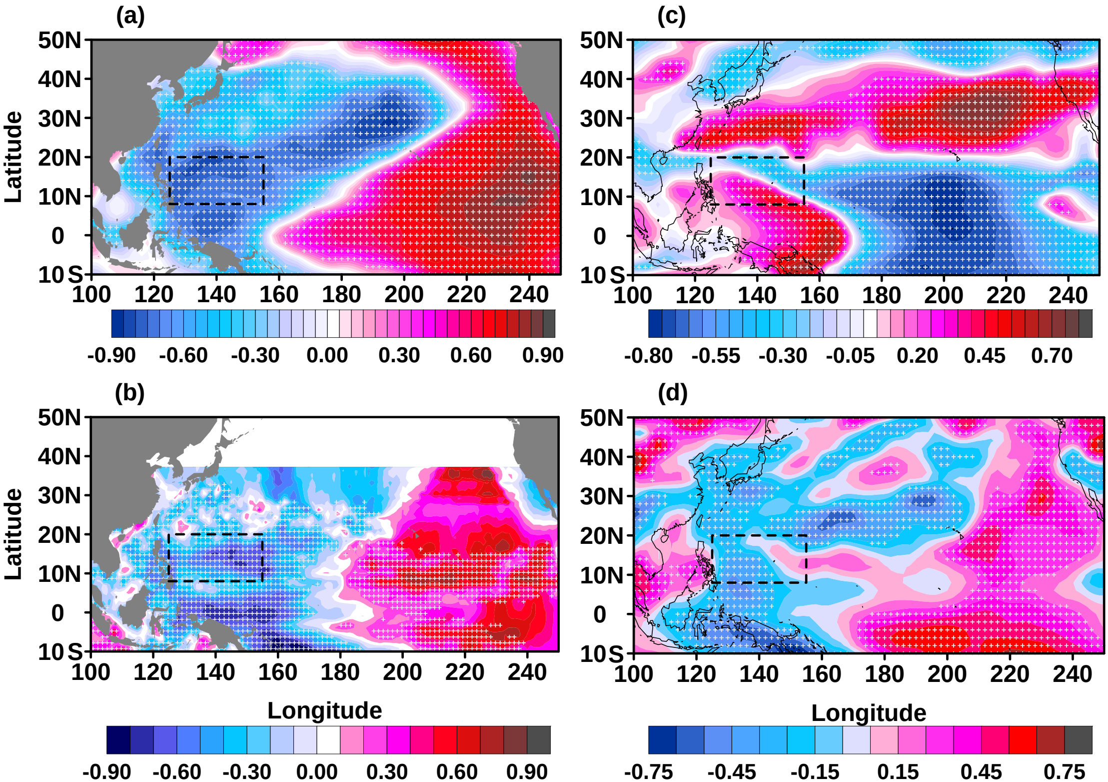

Figure 8. Multidecadal correlation maps between the PDO index and environmental variables (a) SST, (b) TCHP, (c) VWS, and (d) RHUM. The cross sign indicates the statistical significance at the 95% confidence level. Multidecadal variability is obtained to perform a 7-year Gaussian filter to the detrended SST, TCHP, VWS, RHUM fields and the PDO index during May–November. The rectangle box indicates the main RI region.

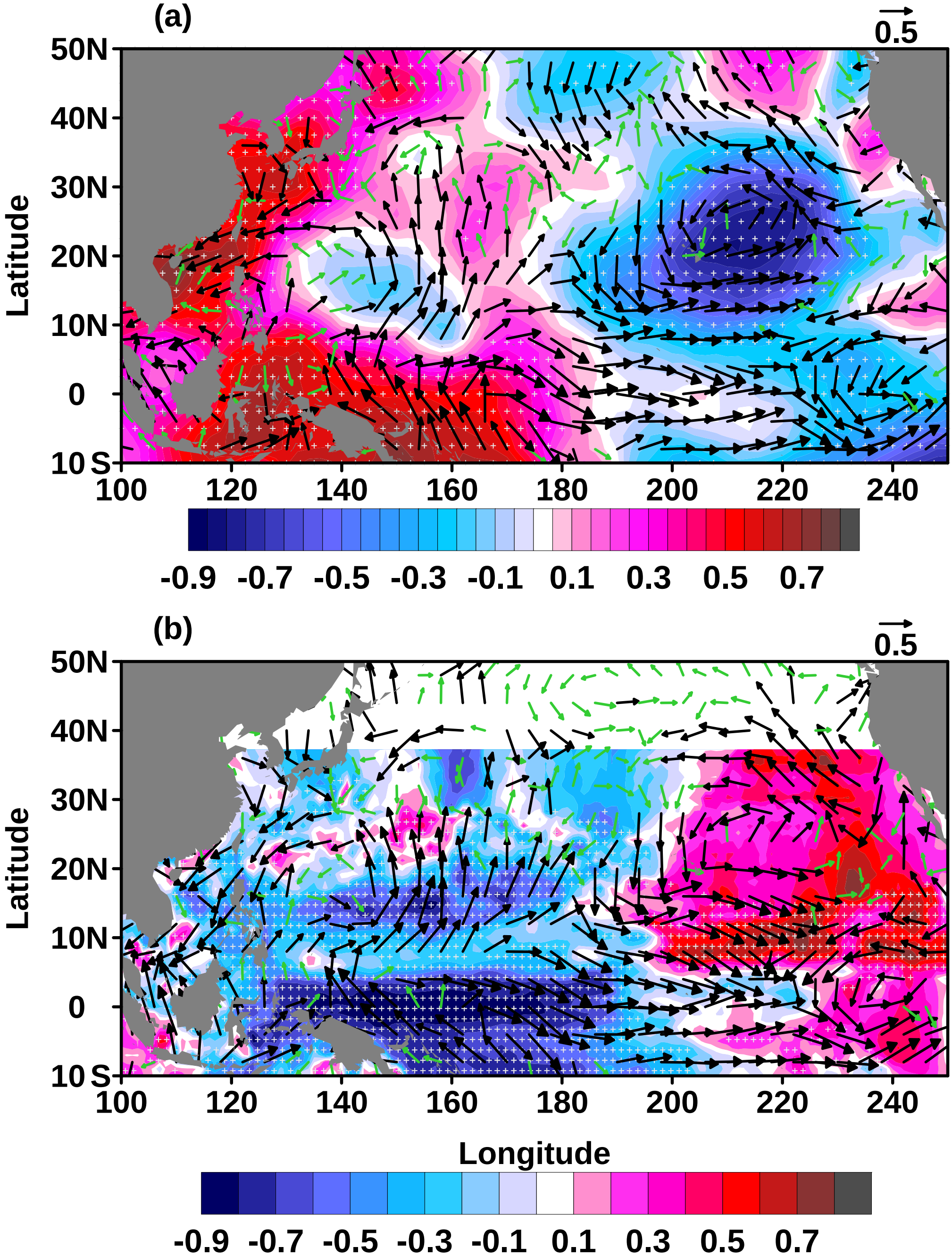

Figure 9. Multidecadal correlation maps between the PDO index and (a) SLP (shaded), 10-m wind (vectors) and (b) D_{26} (shaded), 10-m wind stresses (vectors) during May–November. The cross sign indicates the statistical significance at the 95% confidence level for SLP and D_{26}. The black vectors are statistically significant at the 95% confidence level for wind and wind stress. All variables are smoothed to obtain multidecadal variability by a 7-year Gaussian filter.

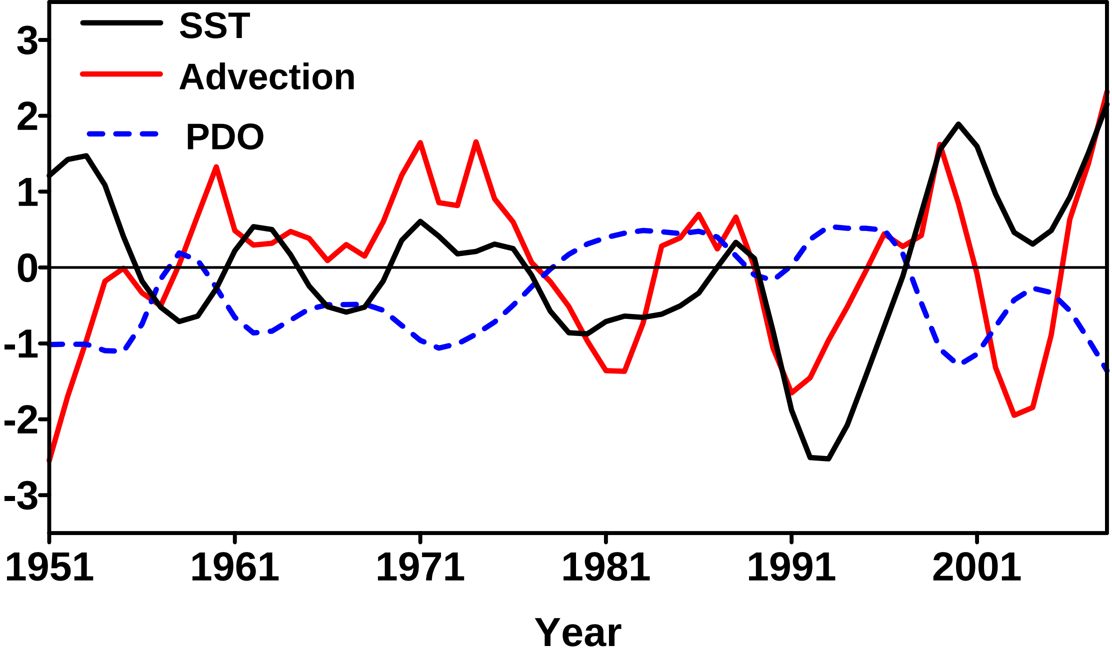

Figure 10. Standardized time series of the region-average SST in the main RI region (8°N–20°N, 125°E–155°E), region-average SST meridional advection in the region of 0–8°N and 125°E–160°E, and PDO index during May–November. Each for the three variables is smoothed to obtain the multidecadal variability by a 7-year Gaussian filter.

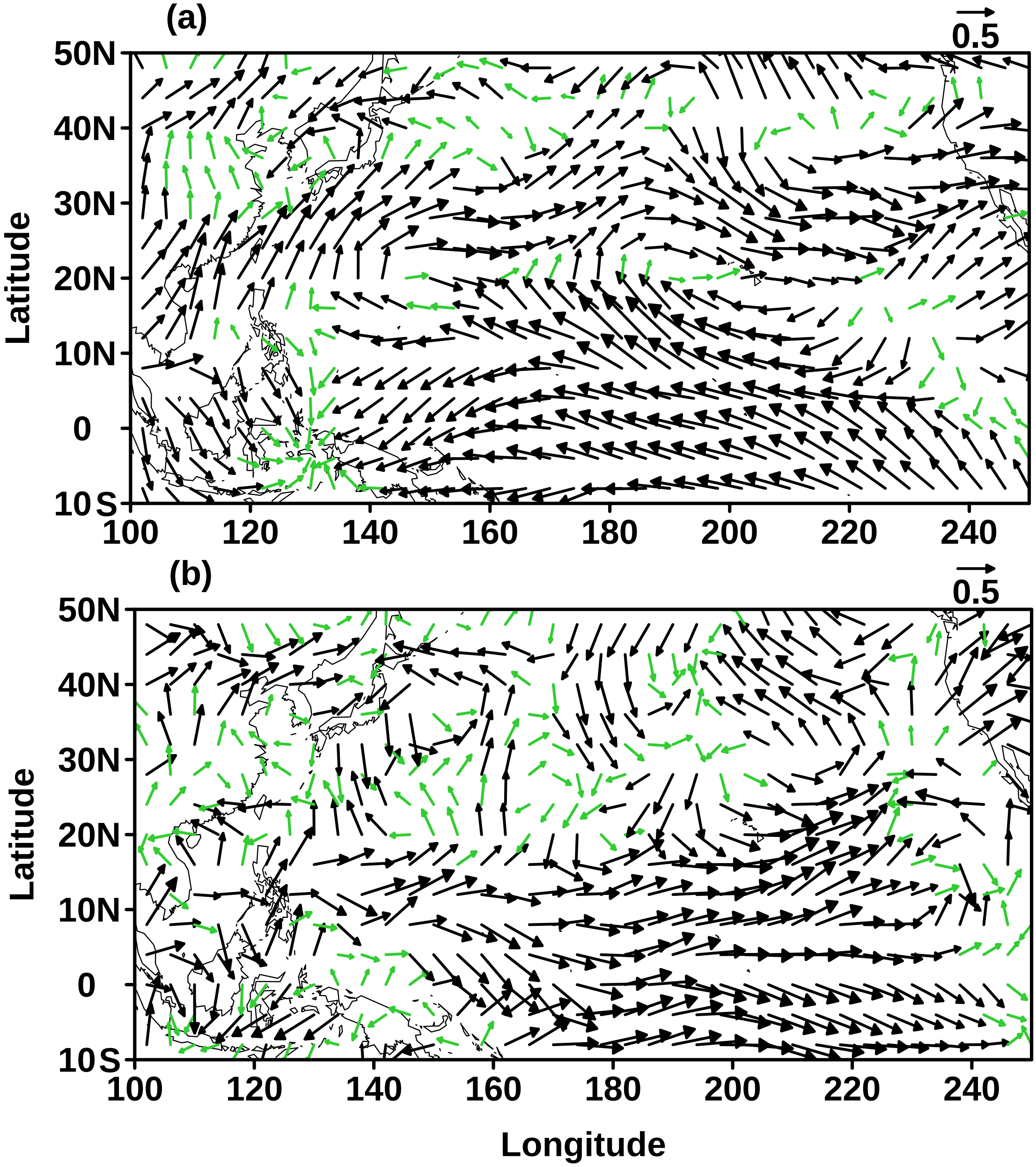

Figure 11. Correlation maps of (a) 200 hPa wind vectors and (b) 850 hPa wind vectors with respect to the PDO index during May–November. The black vectors are statistically significant at the 95% confidence level. All variables are smoothed to obtain multidecadal variability by a 7-year Gaussian filter.